Current Rectification and Photo-Responsive Current Achieved through Interfacial Facet Control of Cu2O−Si Wafer Heterojunctions

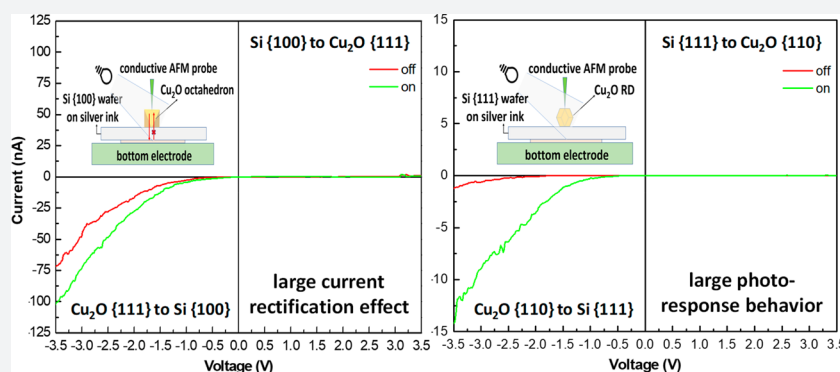An-Ting Lee, Chih-Shan Tan, and Michael H. Huang*

ACCESS | Metrics & More | Article Recommendations | SI Supporting Information

ABSTRACT: Conductive atomic force microscopy (C-AFM) was employed to perform conductivity measurements on a facet-specific Cu2O cube, octahedron, and rhombic dodecahedron and intrinsic Si {100}, {111}, and {110} wafers. Similar I−V curves to those recorded previously using a nanomanipulator were obtained with the exception of high conductivity for the Si {110} wafer. Next, I−V curves of different Cu2O−Si heterostructures were evaluated. Among the nine possible arrangements, Cu2O octahedron/ Si {100} wafer and Cu2O octahedron/Si {110} wafer combinations show good current rectification behaviors. Under white light illumination, Cu2O cube/Si {110} wafer and Cu2O rhombic dodecahedron/Si {111} wafer combinations exhibit the largest degrees of photocurrent, so such interfacial plane-controlled semiconductor heterojunctions with light sensitivity can be applied to make photodetectors. Adjusted band diagrams are presented highlighting different interfacial band bending situations to facilitate or inhibit current flow for different Cu2O−Si junctions. More importantly, the observation of clear current-rectifying effects produced at the semiconductor heterojunctions with properly selected contacting faces or planes implies that novel field-effect transistors (FETs) can be fabricated using this design strategy, which should integrate well with current chip manufacturing processes.

INTRODUCTION

Various semiconductor materials including Cu2O, Ag2O, TiO2, PbS, and SrTiO3 crystals have displayed strongly facet-dependent electrical conductivity properties.[1−7] Ag3PO4 crystals, however, do not possess clear electrical facet effects.[8] Moreover, intrinsic, or undoped, Si, Ge, and GaAs wafers also exhibit large facet dependence in their electrical conductivity responses.[9−11] In the case of Cu2O crystals, the {111}-bound octahedron is highly conductive, but the {110}-terminated rhombic dodecahedron is actually insulating.[1] The {100} faces of a cube is moderately conductive. For Si {100} and {110} wafers, they exhibit normal semiconductor conductivity properties with very low current at applied voltages below 3 V, while Si {111} wafers are much more conductive with current rising within 1 V.[9] Current-rectifying I−V curves resembling those of p−n diode junctions can readily be obtained by making electrical connections to a conductive face and a poorly conductive face of the same crystal or wafer. This field-effect transistor (FET) design can be considered as a first-generation approach. To explain the emergence of the observed electrical facet effects, density functional theory (DFT) calculations have revealed the presence of an ultrathin surface layer (~1 nm or less in thickness) with dissimilar band structures for various surface planes, which should lead to different degrees of surface band bending and facilitate or prevent charge transport across a particular crystal face.[1,3,6,12−15] Furthermore, bond length and bond directions, as well as frontier orbital electron energy distribution, within the thin surface layer can show deviations or variations for the highly conductive crystal faces such as the Si (111) and Cu2O (111) planes, which should yield changes in the surface band structure.[12,13] These DFT results provide a more physical
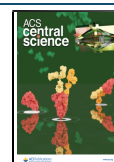
picture of the thin surface layer. Interestingly, the predicted structural deviations in the surface lattice planes may be observable, as seen in the high-resolution transmission electron microscopy (HR-TEM) images of $SrTiO_3$ crystals with slight atomic position deviations and noticeable peak shifts in the X-ray diffraction (XRD) patterns of polyhedral Cu_2O crystals.[7,16] To gain further insights, the most conductive Si and Ge {111} wafers were found to have the lowest surface trap state population and the shortest carrier lifetime, matching with their best electrical conductivity behavior.[17,18] GaAs wafers, however, do not show such surface trap state and carrier lifetime correlation to their conductivity properties.[19]

In addition to surface-related electrical conductivity properties, Cu_2O, Ag_2O, Ag_3PO_4, $SrTiO_3$, and other polyhedral crystals also present strong photocatalytic facet effects.[8,20−24] For example, Cu_2O rhombic dodecahedra are most active toward methyl orange photodegradation, but Cu_2O cubes are simply photocatalytically inert. The idea of a thin surface layer with tunable degrees of band bending was adopted to understand the strong facet dependence in photocatalytic activity. Remarkably, when other semiconductor particles including ZnO, ZnS, CdS, and Ag_3PO_4 are deposited on Cu_2O polyhedra, in many cases, photocatalytic activity suppression to the degree of complete deactivation can happen instead of the expected activity enhancement on the basis of band energy alignment analysis for the semiconductor heterojunctions.[25−27] We can understand these observations because both favorable and mismatched interfacial band bending can happen depending on the contacting lattice planes between the two semiconductor materials. Thus, one can extend the surface layer idea to semiconductor interfaces. Multiple interfacial combinations are possible. In all these heterostructure cases, Cu_2O cubes remain photocatalytically inert, but Ag_2S-decorated Cu_2O cubes show surprisingly good photocatalytic activity, illustrating the unpredictable nature of semiconductor heterojunctions.[28]

Since one knows diverse photocatalytic outcomes are possible for semiconductor heterojunctions, it is natural to think electrical properties of semiconductor heterojunctions with facet control can produce the same current-rectifying effect. The placement of a Cu_2O cube, octahedron, and rhombic dodecahedron on Si {100}, {111}, and {110} wafers gives 9 combinations to investigate. Moreover, if the conductivity measurements can be carried out using a conductive atomic force microscopy (C-AFM) probe, instead of a conventional 4-probe nanomanipulator installed in a scanning electron microscopy (SEM) chamber, the photo-conductivity effect can be performed with additional light illumination. Here, we have first performed electrical conductivity measurements on Cu_2O particles and intrinsic silicon wafers exposing different crystal surfaces, followed by conductivity measurements on the nine combinations of Cu_2O−Si wafer heterostructures. Remarkably, some combinations yield useful current-rectifying properties, while others give notable photocurrent enhancement. The results demonstrate that semiconductor heterojunctions with appropriate interfacial plane control can be explored in the fabrication of transistors and photodetectors.

■ RESULTS AND DISCUSSION

The conductive AFM is a powerful tool for probing electrical properties of nanoscale structures including quantum dots,[29,30] nanorods,[31] and halide perovskites.[32] By using a commercial conductive probe with a typical tip radius of 20 nm as a movable electrode, conductive AFM can provide nanoscale surface structure and electrical behavior. However, the poor positional stability when the probe makes contact with the particle surface can be a problem. With adjustable tip loading force, the peak force (PF) mode can improve contact stability. Equipped with the tunneling module, the tunneling AFM (TUNA) is an advanced C-AFM technique with tunable current sensitivity in the range from fA to μA for I−V measurements. The combination of the PF mode and TUNA, PF-TUNA, is an ideal method for measuring the conductivity of individual nanostructures with high electrical resistance. Here, conductivity measurements were accomplished by using PF-TUNA.

Initially, Cu_2O cubes, octahedra, and rhombic dodecahedra were synthesized following our reported procedures (see the Supporting Information for the experimental detail and Table S1 for a summary of the reagent amounts used).[20,33] SEM images of the synthesized Cu_2O crystals are provided in Figure S1. The particles all possess high shape and size uniformity with sharp faces. The average sizes of the Cu_2O cubes, octahedra, and rhombic dodecahedra are approximately 330, 270, and 265 nm, respectively. For octahedra, the particle size refers to the opposite corner length. For rhombic dodecahedra, opposite face lengths were measured. Figure S1 also shows their XRD patterns, matching exactly to the standard pattern of Cu_2O. Again slight peak shifts can be identified. With respect to the peak positions for rhombic dodecahedra, diffraction peaks for octahedra and cubes are shifted progressively to higher 2θ angles. This phenomenon may arise from the presence of the thin surface layer with bond length deviations. Figure S2 gives XRD patterns of the front and back sides of Si wafers exposing {100}, {110}, and {111} surfaces, confirming their correct crystal orientations.

Since band diagrams of the Cu_2O and Si heterojunctions will be presented to explain the recorded electrical responses, it is useful to first construct band diagrams of different Cu_2O crystals. Figure S3 offers diffuse reflectance spectra of the prepared Cu_2O crystals and the corresponding Tauc plot for band gap determination. The synthesized Cu_2O cubes, octahedra, and rhombic dodecahedra have band gaps of 1.61, 2.17, and 1.84 eV, respectively, showing again that band gap values are still tunable for very large Cu_2O crystals, and light absorption by semiconductors includes both bulk and surface components.[34] Using the band gap values and ultraviolet photoelectron spectroscopy (UPS) results previously obtained for Cu_2O crystals synthesized by the same method for energies of valence band maximum (VBM), Fermi level, and work function, the band diagrams of the prepared Cu_2O cubes, octahedra, and rhombic dodecahedra are presented in Figure S4.[20] When the vacuum level is equalized, there are just small valence band energy differences among the three particle shapes and a small energy difference in the conduction band between octahedra and rhombic dodecahedra. Hence, the conventional band diagrams without regard for the surface effects to band energies cannot explain why Cu_2O octahedra and rhombic dodecahedra show very different electrical properties and why Cu_2O cubes should be photocatalytically inert, while rhombic dodecahedra are far more photocatalytically active than octahedra. Clearly, significant surface band bending should be introduced to address experimental observations.
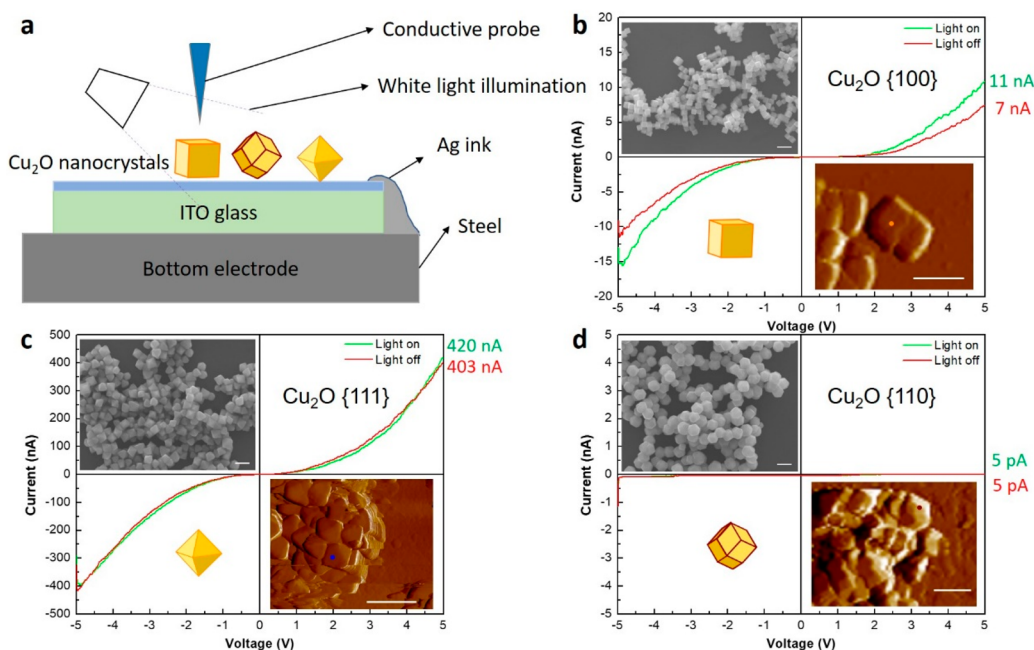
Figure 1. (a) Illustration of the photoresponsive conductivity measurements. The light blue layer represents the deposited Cu_2O crystals. (b−d) Particle SEM and AFM images and the recorded $I-V$ curves for Cu_2O (b) cubes, (c) octahedra, and (d) rhombic dodecahedra with and without light illumination. The dots indicate the measured spots. All scale bars are equal to 500 nm.
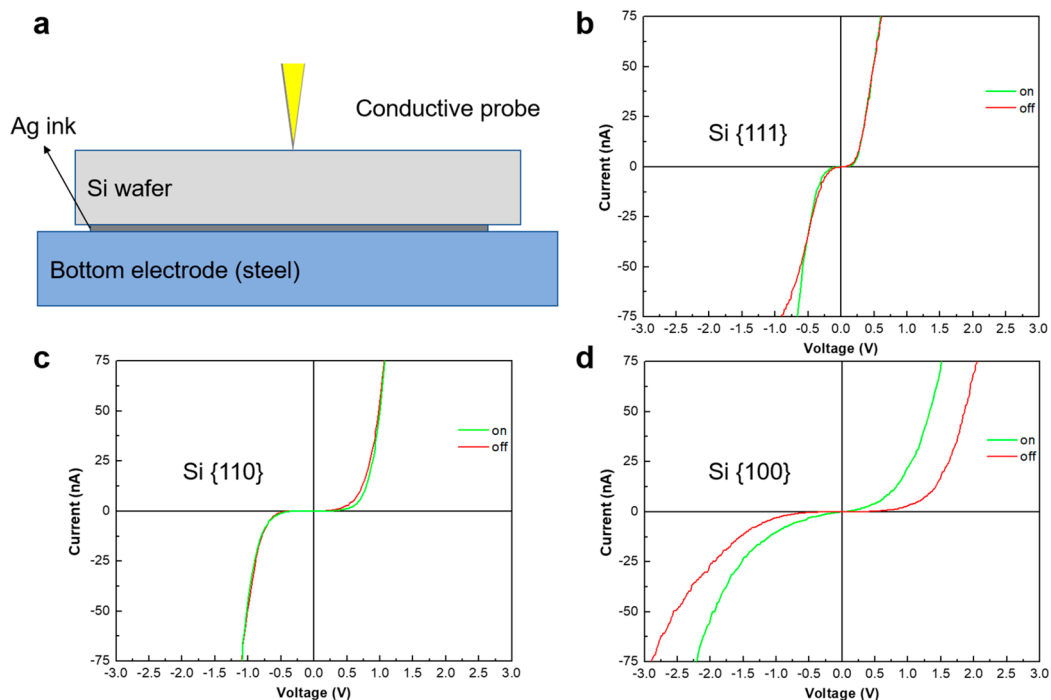
Figure 2. (a) Illustration of the conductivity measurements for Si wafers. (b−d) The recorded $I-V$ curves for Si (b) {111}, (c) {110}, and (d) {100} wafers with and without light illumination.

To ensure that proper electrical connections have been made and the obtained $I-V$ curves are correct, it is necessary to perform conductivity measurements on individual Cu_2O crystals first and see if the recorded $I-V$ curves agree with previous measurements using a nanomanipulator with tungsten probes installed in a SEM chamber. Figure 1 provides a schematic drawing of the sample configuration for electrical conductivity measurements, SEM and AFM images of different Cu_2O crystals, and the recorded $I-V$ curves with and without

LED light illumination. The drawing illustrates that Cu_2O crystals are sandwiched between a conductive probe and an ITO glass, which is electrically connected to the bottom steel electrode using silver ink. The dots in the AFM images indicate the AFM probe contacts for the measured $I-V$ curves. The AFM images reveal that the Cu_2O crystals can be aggregated, so we tried to select a recognizable individual particle with upright orientation as the probe contact points. Each $I-V$ curve represents an average of three continuous measurements.
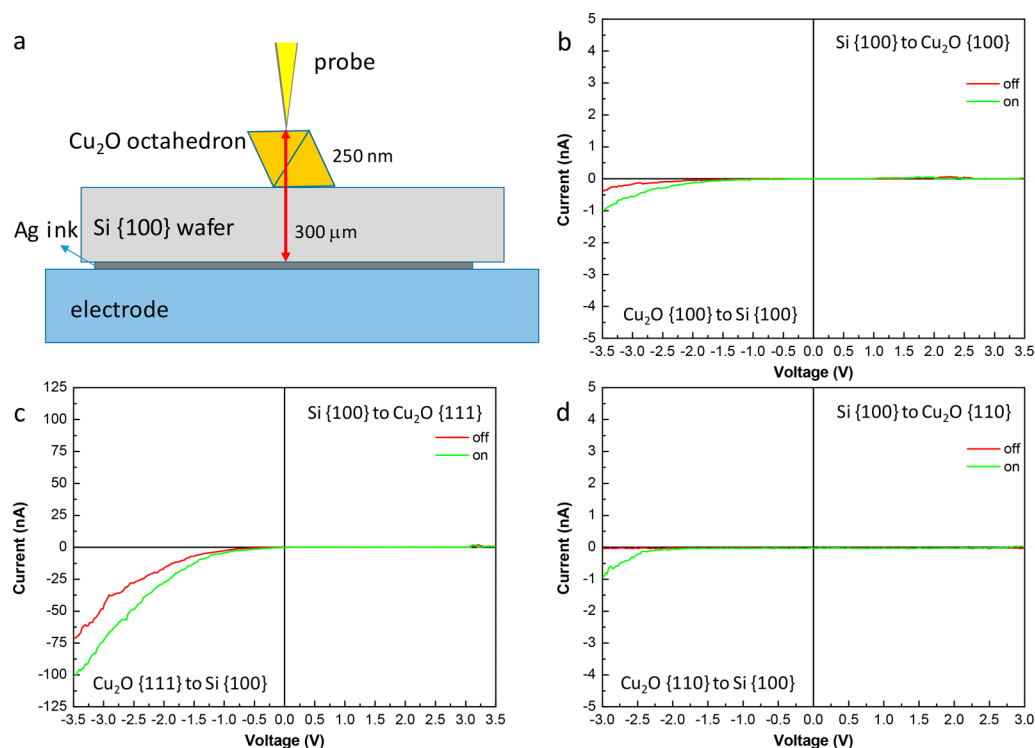
Figure 3. (a) Illustration of using a conductive AFM probe for conductivity measurements of the Cu_2O octahedron/Si {100} wafer heterojunction. (b–d) Measured $I-V$ curves for the (b) Cu_2O cube/Si {100} wafer, (c) Cu_2O octahedron/Si {100} wafer, and (d) Cu_2O rhombic dodecahedron/Si {100} wafer combinations. Current directions are indicated.

In agreement with previous observations, a Cu_2O octahedron is highly conductive with the current reaching 403 nA at 5 V, while a Cu_2O cube only gives a current of 7 nA at 5 V.[1] This is a 57-fold current difference, demonstrating the power of crystal facets to charge transport. The slight asymmetry in the $I-V$ curves should be related to the considerable difference in the two electrode contact area and the electrode composition. A Cu_2O rhombic dodecahedron remains insulating. Thus, the AFM conductivity measurements give similar results to those obtained using tungsten probes. Under light irradiation, the current increases slightly to 420 nA for the octahedron and 11 nA for the cube, but there is no change for the rhombic dodecahedron. The intense light of sufficient energies promotes more electrons to the conduction band and creates holes in the valence band, so photocurrent should generally be improved. The results show that photocurrent enhancement is more pronounced for the less conductive Cu_2O crystals.

Figure 2 is a drawing of the sample configuration for silicon wafer conductivity measurements and the recorded $I-V$ curves with and without light illumination. Each curve represents an average of three continuous measurements. Consistent with the previous observation, the Si {111} wafer is considerably more conductive than the Si {100} wafer.[9] However, the Si {100} wafer actually has fairly good conductivity, and current rises at a lower applied voltage for the Si {110} wafer than for the Si {100} wafer, meaning the Si {110} wafer is more conductive than the Si {100} wafer. Previously, the Si {110} wafer was found to be the least conductive.[9] It is unclear why such a discrepancy exists. A possibility is that the electrode connections are different with tungsten probes on the same side of the wafer. Nevertheless, the new conductivity results should be considered when evaluating the conductivity behaviors of the Cu_2O-Si heterostructures. Upon light

illumination, again, the comparatively less conductive Si {100} wafer displays the largest degree of photocurrent enhancement. The adjusted band diagram with silicon wafers connecting to a Pt electrode is shown in Figure S5. Although intrinsic Si wafers were used, the majority carrier should still be the electrons. Because of the large work function of Pt, a Schottky contact is formed with upward band bending at the interface.[35] The Si {111} wafer and the Pt electrode have the smallest energy difference to indicate its best conductivity. Upon light illumination, a smaller degree of upward band bending can be drawn for the Si {100} wafer to suggest improved conductivity.

Figure 3 depicts the sample configuration of a Cu_2O octahedron on top of a Si {100} wafer for conductivity measurements and the recorded $I-V$ curves of different Cu_2O crystal/Si {100} wafer combinations. Figure S6 provides selected $I-V$ curves for five or more continuous measurements of the Cu_2O octahedron/Si {100} wafer combination to see the current reproducibility. In the positive voltage side of the $I-V$ curve, current flows from the Si wafer to the Cu_2O crystal, while in the negative voltage region, the current direction is from the Cu_2O crystal to the Si wafer through the electrical connection. In the case of a Cu_2O cube on a Si {100} wafer (Figure 3b), slight current-rectifying $I-V$ curves are obtained, and light illumination gives a photocurrent; however, this combination is not useful because of the very small current achieved. Remarkably, the combination of {111}-bound Cu_2O octahedron and Si {100} wafer gives excellent and clean current-rectifying responses with current reaching 75 nA at 3.5 V in the negative voltage region (or in the direction from Pt probe to the bottom electrode) and zero current in the positive voltage region or the opposite direction. Under light irradiation, photocurrent reaching 100 nA was achieved.
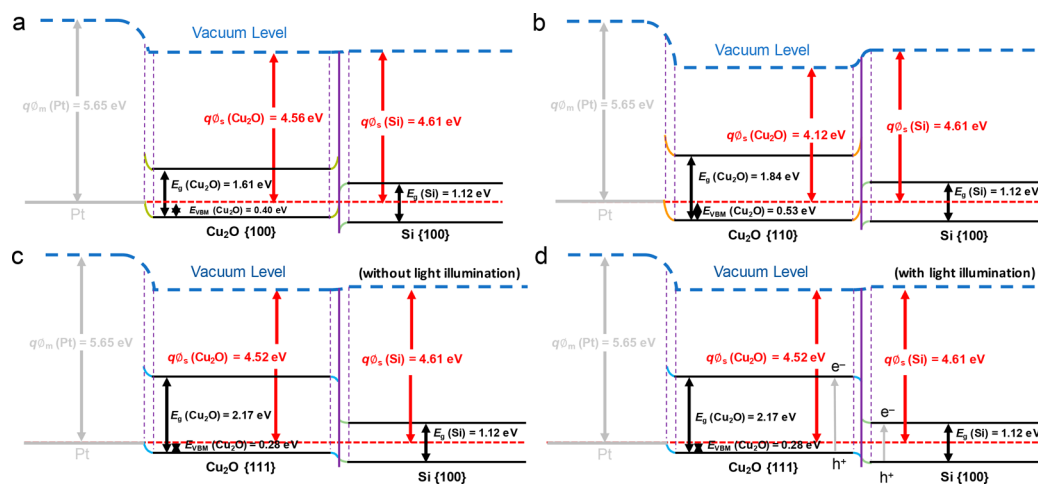
Figure 4. Band diagrams for a Si {100} wafer in contact with (a) a Cu$_2$O cube, (b) a rhombic dodecahedron, and an octahedron (c) without and (d) under white LED illumination.

Considering current has risen sharply beyond 1 V for the Si {100} wafer as seen in Figure 2, this current-rectifying Cu$_2$O {111}/Si {100} combination cannot be predicted from the electrical response of each component. It also suggests that the interfacial band bending situation can change significantly, even when there is no chemical bond formed at the junction. Previously, current-rectifying I−V curves have been observed for Cu$_2$O cubes and octahedra deposited on 1,8-nonadiyne-treated amorphous silicon substrate, so the silicon substrate does not have a well-defined crystal plane.[36−40] Next, the combination of a Cu$_2$O rhombic dodecahedron on a Si {100} wafer did not produce any current (Figure 3d). A small current of 1 nA was observed at 3 V under light illumination. This result seems reasonable, since a Cu$_2$O rhombic dodecahedron is electrically insulating. However, as we will see later, one cannot safely assume that any Cu$_2$O rhombic dodecahedron/Si wafer combination gives no current.

Figure 4 shows the adjusted band diagrams of the three Cu$_2$O/Si {100} wafer combinations to understand the observed electrical behaviors. The Fermi levels for the metal and semiconductors are equalized, but under applied voltages, the Fermi levels can change. Although Cu$_2$O is a p-type semiconductor, the Si wafer is undoped. Because intrinsic Si wafer was used, Fermi level is drawn midway between the valence band and the conduction band. Both electrons and holes can be considered as charge carriers for the band diagrams. In the case of a Cu$_2$O cube with the Si {100} wafer, there is nearly no current. At the Pt−Cu$_2$O junction, upward band bending is drawn to reflect the larger work function of Pt relative to that of Cu$_2$O (Figure 4a). At the heterojunction, the Cu$_2$O {100} face bends upward, and the Si {100} surface bends downward to represent a significant energy barrier to charge migration across this interface. For the Cu$_2$O rhombic dodecahedron case (Figure 4b), a mismatched band bending situation at the semiconductor junction (upward for Cu$_2$O and downward for Si) is drawn to indicate the overall electrically insulating behavior of this heterostructure combination. Under light illumination, current increases negligibly for both the cube and rhombic dodecahedron cases, so the interfacial band bending should not change. In contrast, current flows in the direction from a Cu$_2$O octahedron to the Si {100} wafer (Figure 4c). At the interface, the Cu$_2$O side should bend downward and the Si {100} side bends upward to represent

facile electron migration in the direction from Cu$_2$O to Si. In the reverse current direction, or under the application of a positive voltage, the conduction band energy of Cu$_2$O is at a much higher level than that of Si, so even favorable interfacial band bending would not enable current flow in the direction from the Si {100} wafer to the Cu$_2$O octahedron. The current-rectifying effect then results. Under light illumination, more photoexcited electrons and holes are generated to produce a current increase (Figure 4d).

Figure 5a displays the recorded I−V curves for the Si {111} wafer in contact with a Cu$_2$O cube, octahedron, and rhombic dodecahedron. Current-rectifying effects are observed for the cube case with 8 nA at 3.5 V in the direction from Cu$_2$O to the Si wafer. Current increases moderately to 12.5 V under LED light illumination. Selected I−V curves for five or more continuous measurements of this combination are available in Figure S7. For Cu$_2$O rhombic dodecahedron, a very small current of just 2 nA was observed for the current direction from the Pt probe to the bottom electrode. Remarkably, current rises to 13−14 nA under light illumination. Figure S8 offers I−V curves for three measurements of this combination with and without shining light. Thus, the Cu$_2$O {110}/Si {111} combination can potentially be applied for photon detection with its high light sensitivity. This design employing semiconductor heterojunctions for photodetector application should be a new approach. The considerable photocurrent generation is unexpected, as Cu$_2$O rhombic dodecahedra are not electrically conductive. This example further demonstrates that semiconductor heterojunctions with interfacial plane control can bring unusual and exciting phenomena, as have often been observed in Cu$_2$O-based semiconductor hetero-structures for photocatalytic reactions.[27] For the Cu$_2$O octahedron/Si {111} wafer combination, a very high current has been recorded for both directions, considering both semiconductors are highly conductive. Figure S9 shows the current can reach 200 nA below 2.5 V and below 2 V with the LED light on.

Figure 6 presents band diagrams for a Si {111} wafer in contact with different Cu$_2$O crystals to understand their conductivity behaviors. A favorable interfacial band bending is drawn for the Cu$_2$O cube/Si {111} wafer combination to correspond to its current-rectifying property (Figure 6a). Upon light illumination, photocurrent increases just slightly, so the
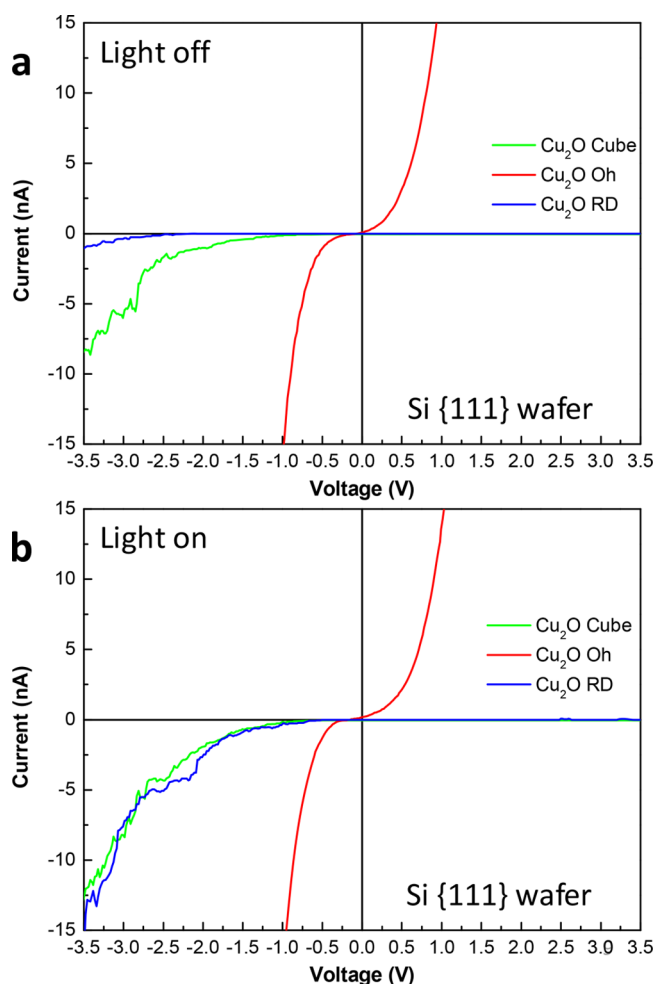
Figure 5. $I-V$ curves recorded for the combinations of a Si {111} wafer with Cu_2O cube, octahedron, and rhombic dodecahedron (a) without and (b) with LED light illumination.

interfacial band bending should look the same. An unmatched interfacial band bending depicts the nearly nonconducting property for the Cu_2O rhombic dodecahedron/Si {111} wafer combination (Figure 6b). Under LED light illumination, however, a large current increase was observed, so the

interfacial band bending becomes favorable (Figure 6c). For the very high conductivity of the Cu_2O octahedron/Si {111} wafer combination, the interfacial band bending should be favorable to charge transport with and without light illumination.

Figure 7 summarizes the $I-V$ curves collected by electrically connecting a Cu_2O cube, octahedron, or rhombic dodecahedron to a Si {110} wafer with and without LED light illumination. Current-rectifying $I-V$ curves were recorded for the Cu_2O cube/Si {110} wafer combination. Additional $I-V$ curves for this combination are provided in Figure S10. Current is about 4 nA at -3 V in the direction from Cu_2O to Si, while the other direction is not conductive. Under light irradiation, current increases to 9 nA, so this combination is also photoresponsive. The combination of a Cu_2O octahedron/Si {110} wafer gives similar current-rectifying $I-V$ curves, but a much larger current of 42 nA was achieved at -3 V, attributed to the higher conductivity of a Cu_2O octahedron. Photoenhanced current goes to 50 nA at -3 V. For the final Cu_2O rhombic dodecahedron/Si {110} wafer combination, there is no current even under light illumination, attributed partly to the insulating nature of a Cu_2O rhombic dodecahedron.

The adjusted band diagrams for the different Cu_2O crystal/Si {110} wafer combinations are shown in Figure S11. A favorable interfacial band bending situation is drawn for the Cu_2O cube/Si {110} wafer combination for its current rectification effect. Under light illumination, more mobile charge carriers are available to produce a larger current. For the complete lack of current, a mismatched interfacial band bending is presented for the Cu_2O rhombic dodecahedron/Si {110} wafer combination. Finally, the Cu_2O octahedron/Si {110} wafer connection gives a matched interfacial band bending to indicate its current-rectifying behavior.

Utilizing the interfacial plane control to achieve current rectification is a new and exciting FET fabrication concept. Figure 8 provides a simple drawing of the FET design. By testing various interfacial combinations between the deposited top semiconductor and the bottom Si or other wafers, it may be possible to find a good semiconductor that meets various electrical response and fabrication requirements. It is envisioned that the top semiconductor can be produced
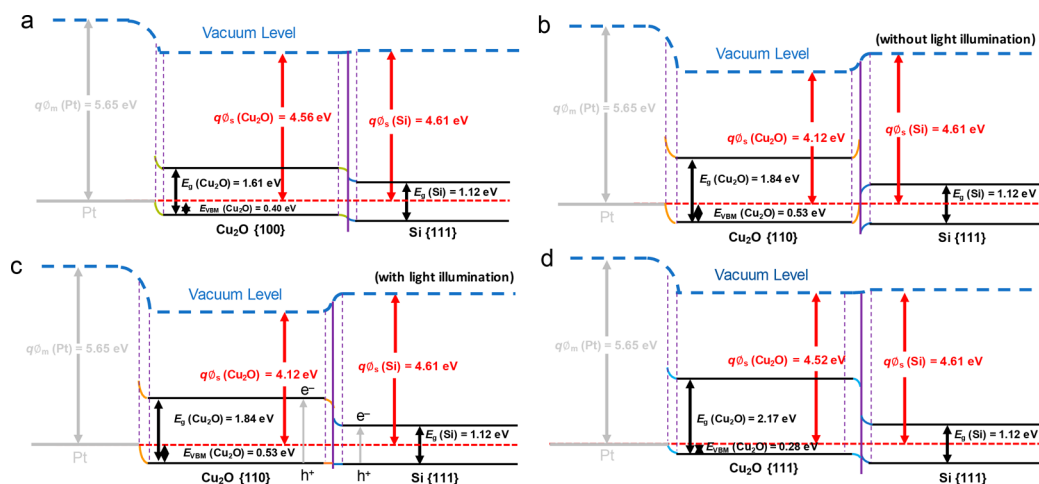
Figure 6. Band diagrams for a Si {111} wafer in contact with (a) a Cu_2O cube, a Cu_2O rhombic dodecahedron (b) without and (c) with LED light illumination, and (d) a Cu_2O octahedron.
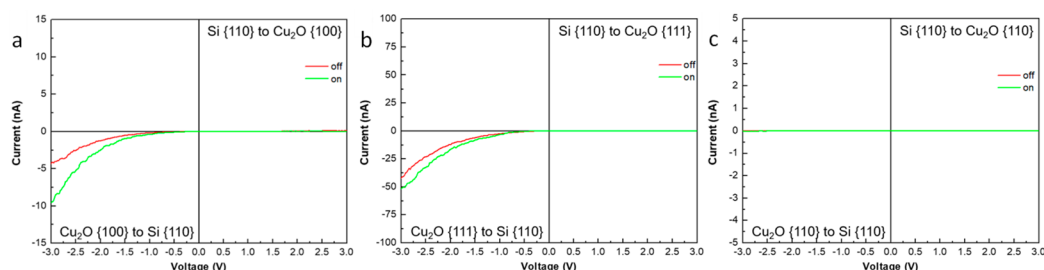
Figure 7. Measured $I-V$ curves for the combinations of a Si {110} wafer and a Cu_2O (a) cube, (b) octahedron, and (c) rhombic dodecahedron. The current directions are indicated.
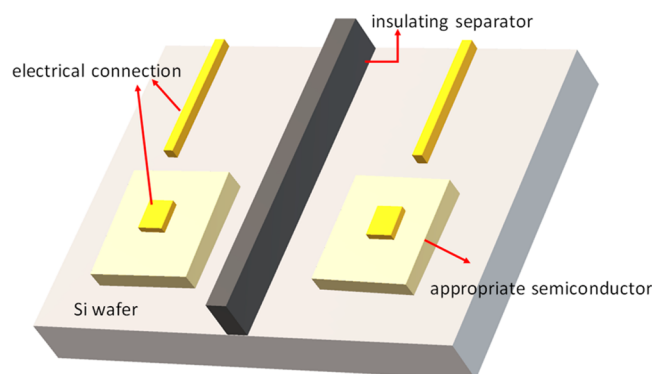
Figure 8. Conceptual design for FETs utilizing the proper combination of a top semiconductor and a Si wafer (or other wafers) with suitable contacting faces or planes to control current flow. The top semiconductor can form through patterned liquid or vapor deposition and can be very thin and small in size. Electrical connections are made to the top semiconductor and the wafer. Current is generated in only one direction under an applied voltage. Some insulating separator may be needed to avoid current crossover.

through a solution or vapor deposition process similar to the patterned photolithography procedure that multiple FETs are made simultaneously on the wafer. The FETs can be made very small and thin with positional control, so they are easier to make than using 2-dimensional materials such as graphene. For example, the reagent-mixed solution can be sprayed onto a patterned substrate to form Cu_2O crystals. Electrical connections are then made to the top semiconductor and bottom Si substrate. Insulating separators may be needed to avoid current crossover. The electrical connection to the top semiconductor at a different height to the substrate needs to be addressed. Previously, it has been proposed that electrical connections to the top and side faces of a Si or Ge wafer exposing different surfaces can be a new FET design.[9,10] We can consider semiconductor heterojunctions as the second-generation FET design, utilizing the current control effects generated at the semiconductor interfaces, which is easier to fabricate. Here, p and n regions are not required. Impurity doping to produce the best electrical performance can be incorporated, since a conventional wafer fabrication process is involved.

CONCLUSION

A conductive AFM approach was used to investigate electrical conductivity behaviors of different Cu_2O crystal/Si wafer heterojunctions to seek proper combinations with current rectification and enhanced photocurrent properties. Initially, conductivity measurements on a Cu_2O cube, octahedron, and

rhombic dodecahedron, as well as Si {100}, {111}, and {110} wafers, were carried out, showing good agreement with the results obtained using a nanomanipulator. However, the Si {110} wafer is much more conductive than observed previously. Among the various Cu_2O crystal/Si wafer heterojunctions, the Cu_2O octahedron/Si {100} wafer and Cu_2O octahedron/Si {110} wafer combinations give good current-rectifying properties. The Cu_2O cube/Si {110} wafer and Cu_2O rhombic dodecahedron/Si {111} wafer combinations exhibit a pronounced photocurrent increase under white LED light illumination for the photodetector application. Some enhanced photocurrent responses were also measured for the Cu_2O octahedron/Si {100} wafer and Cu_2O cube/Si {111} wafer combinations. Adjusted band diagrams showing different interfacial band bending situations to facilitate or inhibit current flow are shown. These results suggest a novel FET design utilizing the current rectification ability of properly selected semiconductor heterojunctions, and the formation of such transistors should fit well with current semiconductor fabrication processes.

EXPERIMENTAL SECTION

Chemicals and Materials. Sodium dodecyl sulfate ($C_{12}H_{25}SO_4Na$, >99%, J. T. Baker), anhydrous copper(II) chloride ($CuCl_2$, 98%, Alfa Aesar), sodium hydroxide (NaOH, 98%, Sigma−Aldrich), hydroxylamine hydrochloride ($NH_2OH \cdot HCl$, 99%, Sigma−Aldrich), and ethanol (C_2H_5OH, 99.8%, Honeywell) were used without further purification. Ultrapure distilled and deionized water (18.2 MΩ) was used for all preparations. Commercial indium tin oxide (ITO) glass (6 μm ITO on 1 mm glass, <10 Ω), colloidal silver (16031, Ted Pella Inc.), a Si (111) wafer (4 in. × 500 μm, R = 16−20 kΩ, double sides polished, Elight), a Si (100) wafer (4 in. × 300 μm, R = 15−20 kΩ, double sides polished, Elight), and a Si (110) wafer (4 in. × 500 μm, R = 20 kΩ, double sides polished, EL-CAT Inc.) were cut and cleaned before the conductivity measurements.

Sample Preparation for Electrical Conductivity Measurements. The synthesized Cu_2O nanocrystal solutions were first diluted to 24 μg/mL with 99.8% ethanol. Next, 5 μL of the diluted solution was dropped onto a commercial ITO glass, and the glass was kept in a desiccator before taking the conductivity measurements. The intrinsic silicon wafers were cut to an area of 1 × 0.8 cm^2, cleaned with acetone for 10 min using an ultrasonicator, and kept in a desiccator. For the combinations of Cu_2O crystals and Si wafers, a drop of the diluted Cu_2O solution was added onto a Si piece, and the wafer was kept in a desiccator before taking the conductivity measurements. No unexpected or unusually high safety hazards were encountered.

For the conductivity measurements of the Cu_2O crystals, an electrical connection was made by smearing conductive silver ink to the side wall of an ITO substrate and to the bottom steel electrode. For the Si wafers, 1 μL of conductive silver ink was added between the Si wafer and the bottom steel electrode without overflow to avoid an unintended side facet contact. For the combinations of Cu_2O crystals on Si wafers, the same method as described for Si wafers was used.

Instrumentation. SEM images of synthesized Cu_2O nanocrystals were obtained using a JEOL JSM-7000F scanning electron microscope. XRD patterns were collected by a Shimadzu XRD-6000 diffractometer using Cu Kα radiation (λ = 1.5418 Å). UV−vis absorption spectra were recorded using a JASCO V-670 spectrophotometer. The conductivity measurements were carried out using a Dimension Icon AFM (Bruker, USA) with a Nanoscope V controller and PF-TUNA module under ambient conditions. A conductive probe was used, which has a Pt/Ir coating with a spring constant of 2 N/m and resonance frequency at 70 kHz (OMCL-AC240TM-R3, Olympus). A white light-emitting diode (LED, XM-L2 U3, CREE) was used as the light source with a power density of ~30 W/cm^2. The lamp was placed at a distance of 10 cm from the sample.

ASSOCIATED CONTENT

Supporting Information

The Supporting Information is available free of charge at https://pubs.acs.org/doi/10.1021/acscentsci.1c01067.

> Procedures for the synthesis of Cu_2O crystals, SEM images, XRD patterns, diffuse reflectance spectra and Tauc plot, band diagrams of different Cu_2O crystals and Si wafers, illustrations and multiple $I-V$ curves of different Cu_2O crystal/Si wafer combinations, and adjusted band diagrams (PDF)

AUTHOR INFORMATION

Corresponding Author

Michael H. Huang − *Department of Chemistry and Frontier Research Center on Fundamental and Applied Sciences of Matters, National Tsing Hua University, Hsinchu 30013, Taiwan;* ⊙ orcid.org/0000-0002-5648-4345; Email: hyhuang@mx.nthu.edu.tw

Authors

An-Ting Lee − *Department of Chemistry and Frontier Research Center on Fundamental and Applied Sciences of Matters, National Tsing Hua University, Hsinchu 30013, Taiwan*

Chih-Shan Tan − *Institute of Electronics, National Yang Ming Chiao Tung University, Hsinchu 30010, Taiwan*

Complete contact information is available at:
https://pubs.acs.org/10.1021/acscentsci.1c01067

Notes

The authors declare no competing financial interest.

ACKNOWLEDGMENTS

REFERENCES

(1) Tan, C.-S.; Hsu, S.-C.; Ke, W.-H.; Chen, L.-J.; Huang, M. H. Facet-Dependent Electrical Conductivity Properties of Cu_2O Crystals. *Nano Lett.* **2015**, *15*, 2155−2160.

(2) Kuo, C.-H.; Yang, Y.-C.; Gwo, S.; Huang, M. H. Facet-Dependent and Au Nanocrystal-Enhanced Electrical and Photocatalytic Properties of Au−Cu_2O Core−Shell Heterostructures. *J. Am. Chem. Soc.* **2011**, *133*, 1052−1057.

(3) Tan, C.-S.; Chen, Y.-J.; Hsia, C.-F.; Huang, M. H. Facet-Dependent Electrical Conductivity Properties of Silver Oxide Crystals. *Chem. - Asian J.* **2017**, *12*, 293−297.

(4) Kim, C. W.; Yeob, S. J.; Cheng, H.-M.; Kang, Y. S. A Selectively Exposed Crystal Facet-Engineered TiO_2 Thin Film Photoanode for the Higher Performance of the Photoelectrochemical Water Splitting Reaction. *Energy Environ. Sci.* **2015**, *8*, 3646−3653.

(5) Liu, G.; Yin, L.-C.; Pan, J.; Li, F.; Wen, L.; Zhen, C.; Cheng, H.-M. Greatly Enhanced Electronic Conduction and Lithium Storage of Faceted TiO_2 Crystals Supported on Metallic Substrates by Tuning Crystallographic Orientation of TiO_2. *Adv. Mater.* **2015**, *27*, 3507−3512.

(6) Tan, C.-S.; Chen, H.-S.; Chiu, C.-Y.; Wu, S.-C.; Chen, L.-J.; Huang, M. H. Facet-Dependent Electrical Conductivity Properties of PbS Nanocrystals. *Chem. Mater.* **2016**, *28*, 1574−1580.

(7) Hsieh, P.-L.; Madasu, M.; Hsiao, C.-H.; Peng, Y.-W.; Chen, L.-J.; Huang, M. H. Facet-Dependent and Adjacent Facet-Related Electrical Conductivity Properties of $SrTiO_3$ Crystals. *J. Phys. Chem. C* **2021**, *125*, 10051−10056.

(8) Hsieh, M.-S.; Su, H.-J.; Hsieh, P.-L.; Chiang, Y.-W.; Huang, M. H. Synthesis of Ag_3PO_4 Crystals with Tunable Shapes for Facet-Dependent Optical Property, Photocatalytic Activity, and Electrical Conductivity Examinations. *ACS Appl. Mater. Interfaces* **2017**, *9*, 39086−39093.

(9) Tan, C.-S.; Hsieh, P.-L.; Chen, L.-J.; Huang, M. H. Silicon Wafers with Facet-Dependent Electrical Conductivity Properties. *Angew. Chem., Int. Ed.* **2017**, *56*, 15339−15343.

(10) Hsieh, P.-L.; Lee, A.-T.; Chen, L.-J.; Huang, M. H. Germanium Wafers Possessing Facet-Dependent Electrical Conductivity Properties. *Angew. Chem., Int. Ed.* **2018**, *57*, 16162−16165.

(11) Hsieh, P.-L.; Wu, S.-H.; Liang, T.-Y.; Chen, L.-J.; Huang, M. H. GaAs Wafers Possessing Facet-Dependent Electrical Conductivity Properties. *J. Mater. Chem. C* **2020**, *8*, 5456−5460.

(12) Tan, C.-S.; Huang, M. H. Surface-Dependent Band Structure Variations and Bond-Level Deviations of Cu_2O. *Inorg. Chem. Front.* **2021**, *8*, 4200−4208.

(13) Tan, C.-S.; Huang, M. H. Metal-like Band Structures of Ultrathin Si {111} and {112} Surface Layers Revealed through Density Functional Theory Calculations. *Chem. - Eur. J.* **2017**, *23*, 11866−11871.

(14) Tan, C.-S.; Huang, M. H. Density Functional Theory Calculations Revealing Metal-like Band Structures for Ultrathin Ge {111} and {211} Surface Layers. *Chem. - Asian J.* **2018**, *13*, 1972−1976.

(15) Tan, C.-S.; Huang, M. H. Density Functional Theory Calculations Revealing Metal-like Band Structures and Work Function Variation for Ultrathin Gallium Arsenide (111) Surface Layers. *Chem. - Asian J.* **2019**, *14*, 2316−2321.

(16) Madasu, M.; Huang, M. H. Cu_2O Polyhedra for Aryl Alkyne Homocoupling Reactions. *Catal. Sci. Technol.* **2020**, *10*, 6948−6952.

(17) Tan, C.-S.; Zhao, Y.; Guo, R.-H.; Chuang, W.-T.; Chen, L.-J.; Huang, M. H. Facet-Dependent Surface Trap States and Carrier Lifetimes of Silicon. *Nano Lett.* **2020**, *20*, 1952−1958.

(18) Tan, C.-S.; Lu, M.-Y.; Peng, W.-H.; Chen, L.-J.; Huang, M. H. Germanium Possessing Facet-Specific Trap States and Carrier Lifetimes. *J. Phys. Chem. C* **2020**, *124*, 13304−13309.

(19) Tan, C.-S.; Chen, L.-J.; Huang, M. H. Large Facet-Specific Built-in Potential Differences Affecting Trap State Densities and Carrier Lifetimes of GaAs Wafers. *J. Phys. Chem. C* **2020**, *124*, 21577−21582.

(20) Chu, C.-Y.; Huang, M. H. Facet-Dependent Photocatalytic Properties of Cu_2O Crystals Probed by Electron, Hole and Radical Scavengers. *J. Mater. Chem. A* **2017**, *5*, 15116–15123.

(21) Zhang, Y.; Deng, B.; Zhang, T.; Gao, D.; Xu, A.-W. Shape Effects of Cu_2O Microcrystals on Photocatalytic Activity. *J. Phys. Chem. C* **2010**, *114*, 5073–5079.

(22) Chen, Y.-J.; Chiang, Y.-W.; Huang, M. H. Synthesis of Diverse Ag_2O Crystals and Their Facet-Dependent Photocatalytic Activity Examination. *ACS Appl. Mater. Interfaces* **2016**, *8*, 19672–19679.

(23) Hsieh, P.-L.; Naresh, G.; Huang, Y.-S.; Tsao, C.-W.; Hsu, Y.-J.; Chen, L.-J.; Huang, M. H. Shape-Tunable $SrTiO_3$ Crystals Revealing Facet-Dependent Optical and Photocatalytic Properties. *J. Phys. Chem. C* **2019**, *123*, 13664–13671.

(24) Huang, M. H.; Naresh, G.; Chen, H.-S. Facet-Dependent Electrical, Photocatalytic, and Optical Properties of Semiconductor Crystals and Their Implications for Applications. *ACS Appl. Mater. Interfaces* **2018**, *10*, 4–15.

(25) Naresh, G.; Hsieh, P.-L.; Meena, V.; Lee, S.-K.; Chiu, Y.-H.; Madasu, M.; Lee, A.-T.; Tsai, H.-Y.; Lai, T.-H.; Hsu, Y.-J.; Lo, Y.-C.; Huang, M. H. Facet-Dependent Photocatalytic Behaviors of ZnS-Decorated Cu_2O Polyhedra Arising from Tunable Interfacial Band Alignment. *ACS Appl. Mater. Interfaces* **2019**, *11*, 3582–3589.

(26) Naresh, G.; Lee, A.-T.; Meena, V.; Satyanarayana, M.; Huang, M. H. Photocatalytic Activity Suppression of Ag_3PO_4-Decorated Cu_2O Octahedra and Rhombic Dodecahedra. *J. Phys. Chem. C* **2019**, *123*, 2314–2320.

(27) Huang, M. H.; Madasu, M. Facet-Dependent and Interfacial Plane-Related Photocatalytic Behaviors of Semiconductor Nanocrystals and Heterostructures. *Nano Today* **2019**, *28*, 100768.

(28) Liang, T.-Y.; Chan, S.-J.; Patra, A. S.; Hsieh, P.-L.; Chen, Y.-A.; Ma, H.-H.; Huang, M. H. Inactive Cu_2O Cubes Become Highly Photocatalytically Active with Ag_2S Deposition. *ACS Appl. Mater. Interfaces* **2021**, *13*, 11515–11523.

(29) Mocatta, D.; Cohen, G.; Schattner, J.; Millo, O.; Rabani, E.; Banin, U. Heavily Doped Semiconductor Nanocrystal Quantum Dots. *Science* **2011**, *332*, 77–81.

(30) Jiang, X.; Liu, H.; Zhang, X.; Cheng, G.; Wang, S.; Du, Z. A Direct Investigation of Photocharge Transfer across Monomolecular Layer between C_{60} and CdS Quantum Dots by Photoassisted Conductive Atomic Force Microscopy. *AIP Adv.* **2016**, *6*, 045012.

(31) Beinik, I.; Kratzer, M.; Wachauer, A.; Wang, L.; Lechner, R. T.; Teichert, C.; Motz, C.; Anwand, W.; Brauer, G.; Chen, X. Y.; Hsu, X. Y.; Djurišić, A. B. Electrical Properties of ZnO Nanorods Studied by Conductive Atomic Force Microscopy. *J. Appl. Phys.* **2011**, *110*, 052005.

(32) Ma, J.-Y.; Ding, J.; Yan, H.-J.; Wang, D.; Hu, J.-S. Temperature-Dependent Local Electrical Properties of Organic–Inorganic Halide Perovskites: In Situ KPFM and c-AFM Investigation. *ACS Appl. Mater. Interfaces* **2019**, *11*, 21627–21633.

(33) Wu, S.-C.; Tan, C.-S.; Huang, M. H. Strong Facet Effects on Interfacial Charge Transfer Revealed through the Examination of Photocatalytic Activities of Various Cu_2O–ZnO Heterostructures. *Adv. Funct. Mater.* **2017**, *27*, 1604635.

(34) Huang, M. H. Semiconductor Nanocrystals Possessing Broadly Size- and Facet-Dependent Optical Properties. *J. Chin. Chem. Soc.* **2021**, *68*, 45–50.

(35) Jiang, C.; Moniz, S. J. A.; Wang, A.; Zhang, T.; Tang, J. Photoelectrochemical Devices for Solar Water Splitting – Materials and Challenges. *Chem. Soc. Rev.* **2017**, *46*, 4645–4660.

(36) Vogel, Y. B.; Gonçales, V. R.; Al-Obaidi, L.; Gooding, J. J.; Darwish, N.; Ciampi, S. Nanocrystal Inks: Photoelectrochemical Printing of Cu_2O Nanocrystals on Silicon with SD Control on Polyhedral Shapes. *Adv. Funct. Mater.* **2018**, *28*, 1804791.

(37) Vogel, Y. B.; Zhang, J.; Darwish, N.; Ciampi, S. Switching of Current Rectification Ratios within a Single Nanocrystal by Facet-Resolved Electrical Wiring. *ACS Nano* **2018**, *12*, 8071–8080.

(38) Vogel, Y. B.; Gonçales, V. R.; Gooding, J. J.; Ciampi, S. Electrochemical Microscopy Based on Spatial Light Modulators: A Projection System to Spatially Address Electrochemical Reactions at Semiconductors. *J. Electrochem. Soc.* **2018**, *165*, H3085–H3092.

(39) Zhang, S.; Ferrie, S.; Lyu, X.; Xia, Y.; Darwish, N.; Wang, Z.; Ciampi, S. Absence of a Relationship between Surface Conductivity and Electrochemical Rates: Redox-Active Monolayers on Si(211), Si(111), and Si (110). *J. Phys. Chem. C* **2021**, *125*, 18197–18203.

(40) Zhang, S.; Ferrie, S.; Peiris, C. R.; Lyu, X.; Vogel, Y. B.; Darwish, N.; Ciampi, S. Common Background Signals in Voltammograms of Crystalline Silicon Electrodes are Reversible Silica–Silicon Redox Chemistry at Highly Conductive Surface Sites. *J. Am. Chem. Soc.* **2021**, *143*, 1267–1272.